Modelling Passive Diastolic Filling of the Left Ventricle

Diogo Amaro

NOVA School of Science and Technology, Department of Physics

October 28, 2025

Abstract

The objective of this report is to describe the mathematical formulation of the passive diastolic filling of the left ventricle, as well as its implementation using finite element discretization. The report begins with an overview of the physiological background of diastolic filling, followed by a detailed description of the governing equations and boundary conditions. Next we solve the weak form of the governing equations, leading to a formulation of the problem that is suitable for numerical implementation. The weak solution is then presented and discussed, along with numerical results demonstrating the model's ability to capture key biomechanical behaviors of the left ventricle during diastole.

1 Introduction

The mechanical behavior of the left ventricle (LV) during passive diastolic filling can be formulated as a quasi-static boundary value problem governed by the equilibrium of a hyperelastic, nearly incompressible solid. Let $\Omega \subset \mathbb{R}^3$ denote the current configuration of the ventricular domain with boundary $\partial\Omega = \Gamma^D \cup \Gamma^N$, where $\Gamma^D \cap \Gamma^N = \emptyset$. The displacement field $\mathbf{u} : \Omega \to \mathbb{R}^3$ satisfies the balance of linear momentum

$$\nabla \cdot \boldsymbol{\sigma}(\mathbf{u}) + \mathbf{b} = \mathbf{0} \quad \text{in } \Omega, \tag{1.1}$$

subject to the Dirichlet and Neumann boundary conditions

$$\mathbf{u} = \mathbf{u}_0 \quad \text{on } \Gamma^D, \qquad \boldsymbol{\sigma}(\mathbf{u}) \cdot \mathbf{n} = \mathbf{t} \quad \text{on } \Gamma^N, \tag{1.2}$$

where $\boldsymbol{\sigma}$ denotes the Cauchy stress tensor, $\mathbf{b}$ the body force per unit volume, and $\mathbf{n}$ the unit outward normal to $\partial\Omega$.

The constitutive behavior of the myocardium is modeled through an incompressible invariant-based constitutive law, formulated by Holzapfel and Odgen. The so called H-O model [1] defines a strain-energy density function Ψ, where

$$\begin{aligned}
\Psi = &\frac{a}{2b}\exp[b(I_1 - 3)] - 1 \\
&+ \sum_{i \in \{\text{f,s}\}} \frac{a_1}{2b_i}\exp[b_i(I_{4i} - 1)^2] - 1 \\
&+ \frac{a_{\text{fs}}}{2b_{\text{fs}}}\exp(b_{\text{fs}}I_{8\text{fs}}^2 - 1),
\end{aligned} \tag{1.3}$$

in which $\mathbf{q} = (a, b, a_\text{f}, b_\text{f}, a_\text{s}, b_\text{s}, a_\text{fs}, b_\text{fs})$ are eight positive unknown material parameters and I_1, I_{4i} and $I_{8\text{fs}}$ are the invariants associated with each direction of the local coordinate system $\mathbf{f}$–$\mathbf{s}$–$\mathbf{n}$:

$$\begin{cases} I_1 = \text{tr}(\mathbf{C}), & I_{4\text{f}} = \mathbf{f}_0 \cdot (\mathbf{C}\mathbf{f}_0), \\ I_{4\text{s}} = \mathbf{s}_0 \cdot (\mathbf{C}\mathbf{s}_0), & I_{8\text{fs}} = \mathbf{f}_0 \cdot (\mathbf{C}\mathbf{s}_0), \end{cases} \tag{1.4}$$

in which f_0 and s_0 are the myofibre and sheet orientations in the reference configuration, which are known before the simulations. The right Cauchy-Green deformation tensor $\mathbf{C}$ is defined as $\mathbf{C} = \mathbf{F}^\top \mathbf{F}$, and $\mathbf{F}$ is the deformation gradient

$$\mathbf{F} = \mathbf{I} + \frac{\partial \mathbf{u}}{\partial \mathbf{X}}, \tag{1.5}$$

where $\mathbf{I}$ is the identity tensor, $\mathbf{u}$ is the displacement vector and $\mathbf{X}$ is the position vector in the reference configuration.

Assuming a hyperelastic response, we can then define the stress as

$$\boldsymbol{\sigma} = \frac{2}{J} \mathbf{F} \frac{\partial \Psi}{\partial \mathbf{C}} \mathbf{F}^\top, \qquad J = \det(\mathbf{F}), \tag{1.6}$$

where incompressibility is weakly enforced through a volumetric penalty, derived from the decomposition of the deformation gradient $\mathbf{F}$ into a volumetric part and an isochoric (distortional) part. For further details, the reader is directed to [1, 2].

The strong form (1.1) admits a weak formulation, i.e., find $\mathbf{u} \in V$ such that

$$a(\mathbf{u}, \mathbf{v}) = L(\mathbf{v}) \quad \forall \mathbf{v} \in V_0, \tag{1.7}$$

where

$$a(\mathbf{u}, \mathbf{v}) = \int_\Omega \boldsymbol{\sigma}(\mathbf{u}) : \nabla \mathbf{v} \, d\Omega, \qquad L(\mathbf{v}) = \int_\Omega \mathbf{b} \cdot \mathbf{v} \, d\Omega + \int_{\Gamma^N} \mathbf{t} \cdot \mathbf{v} \, d\Gamma,$$

and V, $V_0 \subset [H^1(\Omega)]^3$ are appropriate Sobolev spaces incorporating the essential boundary conditions.

Under standard assumptions on the material model and geometry, the bilinear form $a(\cdot, \cdot)$ is continuous and coercive on V_0, ensuring existence and uniqueness of the weak solution by the Lax–Milgram theorem. The finite element approximation $\mathbf{u}_h \in V_h \subset V$ inherits these properties, and standard Céa's lemma arguments yield the convergence estimate

$$\|\mathbf{u} - \mathbf{u}_h\|_V \leq C \inf_{\mathbf{v}_h \in V_h} \|\mathbf{u} - \mathbf{v}_h\|_V. \tag{1.8}$$

This paper demonstrates the implementation of the variational formulation (1.7) in `FEniCS`, illustrating how to numerically solve the passive diastolic filling problem using finite element discretization.

2 Constitutive Modelling of Passive Myocardium

The purpose of this section is to provide a mathematical description of the constitutive model used to characterize the mechanical behavior of the myocardium during passive diastolic filling. To this end, an overview of the fundamentals of soft tissue mechanics is presented, including the continuum mechanical framework, relevant kinematic and kinetic measures, and conservation laws.

2.1 Continuum Mechanics

Continuum mechanics is founded on the concept that a material (fluid, solid, or mixture) and its properties can be approximated by fields that are well defined almost everywhere [3, 4, 5]. This continuum assumption considers the scale at which discrete microstructural variations appear to much smaller than the smallest scales of interest. This enables the averaging of material characteristics, transforming the discrete nature of materials into well-defined point-wise fields. Conservation laws can be derived to enable computational simulations of heart tissue, detailing its movement, deformation (kinematics), and stress responses (kinetics). This section briefly reviews these concepts.

2.1.1 Kinematics of Large Deformation

Kinematics is the study of motion of particles or objects and its subsequent deformation without reference to the cause, i.e., without explicit consideration of the masses and forces involved [6]. To describe the motion of a body in a d-dimensional space, we define the region occupied by the body at $t = t_0$ as $\Omega_0 \subset \mathbb{R}^d$, to which we refer to as the *reference configuration*. The choice of a reference configuration is completely arbitrary[1]. Consequently, reference coordinates $\mathbf{X} \in \Omega_0$ describe the undeformed position of material particles within the body. In response to deformations, the material particles move to the coordinates $\mathbf{x} \in \Omega(t)$ at some time t, to which we refer to as the *current configuration*. Assuming that the reference coordinates, $\mathbf{X}$, and physical coordinates, $\mathbf{x}$, are related by a continuous displacement field $\mathbf{u}(\mathbf{X}, t)$, i.e., $\mathbf{x}(\mathbf{X}, t) = \mathbf{u}(\mathbf{X}, t) + \mathbf{X}$, we can then define the Jacobian of the mapping relative to the reference configuration, also known as the deformation gradient tensor, as

$$\mathbf{F} = \frac{\partial \mathbf{x}}{\partial \mathbf{X}} = \nabla_{\mathbf{X}} \mathbf{u} + \mathbf{I}, \tag{2.1}$$

or, in Cartesian components, as

$$F_{ij} = \frac{\partial u_i}{\partial X_j} + \delta_{ij}, \tag{2.2}$$

where $\mathbf{I}$ is the identity tensor, with components described by the Kronecker delta symbol.

$$\delta_{ij} = \begin{cases} 1, & \text{if } i = j, \\ 0, & \text{if } i \neq j. \end{cases} \tag{2.3}$$

For the description of local kinematics of any deformable body, we use the standard notation and convention

$$J = \det \mathbf{F} > 0. \tag{2.4}$$

Because J quantifies the local change in volume, then for an incompressible material, the constraint

$$J = \det \mathbf{F} \equiv 1 \tag{2.5}$$

must hold true.

The concepts of displacement field and deformation gradient are introduced to quantify the change in shape of infinitesimal line elements in a solid body [6]. To see this, let us draw a straight (red dashed) line on the undeformed configuration of a solid, as shown in Figure 1.

---

[1]More generally, any configuration that the body is capable of occupying (irrespective of whether it actually does or not) may serve as a reference configuration.
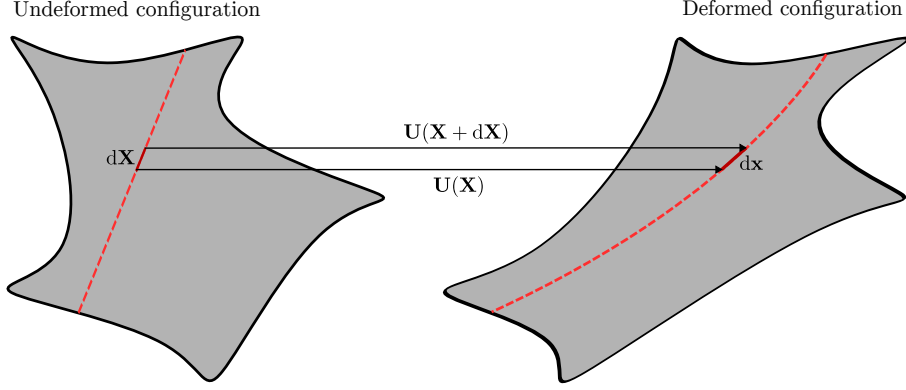
Figure 1: Visualization of an infinitesimal line element in a deforming solid body. A reference straight line (dashed red) drawn on the undeformed configuration becomes a smooth curve upon deformation. However, a sufficiently small segment of this line, $\mathrm{d}\mathbf{X}$, remains approximately straight after deformation, mapping to $\mathrm{d}\mathbf{x}$ through the displacement field given by $\mathbf{U}(\mathbf{X} + \mathrm{d}\mathbf{X}) - \mathbf{U}(\mathbf{X})$. This shows that despite global curvature, local material behavior can be captured by stretch and rotation only.

The line would be mapped to a smooth curve on the deformed configuration. However, suppose we focus on a line segment $\mathrm{d}\mathbf{X}$, much shorter than the radius of curvature of this curve, as shown in Fig. 1. The segment would be straight in the undeformed configuration, and would also be (almost) straight in the deformed configuration. Thus, no matter how complex a deformation we impose on a solid, infinitesimal line segments are merely stretched and rotated by a deformation. We can then define the relation between infinitesimal line segments $\mathrm{d}\mathbf{X}$ and $\mathrm{d}\mathbf{x}$ as

$$\mathrm{d}\mathbf{x} = \mathbf{F} \cdot \mathrm{d}\mathbf{X}, \qquad \mathrm{d}x_i = F_{ik} \cdot \mathrm{d}X_k. \tag{2.6}$$

Written out as a matrix equation, we have

$$\begin{bmatrix} dx_1 \\ dx_2 \\ dx_3 \end{bmatrix} = \begin{bmatrix} 1 + \dfrac{\partial u_1}{\partial X_1} & \dfrac{\partial u_1}{\partial X_2} & \dfrac{\partial u_1}{\partial X_3} \\ \dfrac{\partial u_2}{\partial X_1} & 1 + \dfrac{\partial u_2}{\partial X_2} & \dfrac{\partial u_2}{\partial X_3} \\ \dfrac{\partial u_3}{\partial X_1} & \dfrac{\partial u_3}{\partial X_2} & 1 + \dfrac{\partial u_3}{\partial X_3} \end{bmatrix} \begin{bmatrix} dX_1 \\ dX_2 \\ dX_3 \end{bmatrix} \tag{2.7}$$

Following this logic, if a material fiber of initial length l_0 oriented along a unit vector $\mathbf{N}$ in the undeformed configuration, i.e. $\mathrm{d}\mathbf{X} = l_0\mathbf{N}$, is stretched and rotated into a fiber of current length l and orientation $\mathbf{n}$ in the deformed configuration, i.e. $\mathrm{d}\mathbf{x} = l\mathbf{n}$, then we can quantify the squared length of infinitesimal fibers in the deformed configuration through the deformation tensors as

$$||\mathrm{d}\mathbf{x}||^2 = \frac{l^2}{l_0^2} = \mathbf{N} \cdot \mathbf{C} \cdot \mathbf{N}, \tag{2.8}$$

$$||\mathrm{d}\mathbf{X}||^2 = \frac{l_0^2}{l^2} = \mathbf{n} \cdot \mathbf{B}^{-1} \cdot \mathbf{n}. \tag{2.9}$$

Here, $\mathbf{C}$ and $\mathbf{B}$ are the right and left Cauchy–Green deformation tensors, defined respectively as:

$$\mathbf{C} = \mathbf{F}^{\mathrm{T}} \cdot \mathbf{F}, \qquad C_{ij} = F_{ki} \cdot F_{kj}, \tag{2.10}$$

$$\mathbf{B} = \mathbf{F} \cdot \mathbf{F}^{\mathrm{T}}, \qquad B_{ij} = F_{ik} \cdot F_{jk}. \tag{2.11}$$

4

Both $\mathbf{C}$ and $\mathbf{B}$ are tensorial quantities used to model highly deformable solids such as the cardiac tissue and provide information about the local and directionally dependent stretch behavior of the material. Another commonly used kinematic quantity is the Green–Lagrange strain tensor, $\mathbf{E}$, that evaluates how much a given displacement differs locally from a rigid body displacement [7]:

$$\mathbf{E} = \frac{1}{2}(\mathbf{C} - \mathbf{I}), \qquad E_{ij} = \frac{1}{2}(C_{ij} - \delta_{ij}). \tag{2.12}$$

The development of a constitutive model requires coordinate independence and rigid body invariance [8, 9]. In order to account for those requirements, we define the principal invariants of $\mathbf{C}$ (and also of $\mathbf{B}$) as

$$I_1 = \mathrm{trace}\,(\mathbf{C}), \qquad I_2 = \frac{1}{2}[I_1^2 - \mathrm{trace}(\mathbf{C}^2)] \quad \text{and} \quad I_3 = \det \mathbf{C}, \tag{2.13}$$

where $I_3 = J^2 = 1$ for an incompressible material[2]. These invariants, however, model isotropic materials. Because the cardiac tissue is anisotropic, additional pseudo-invariants must be defined for directional dependence [10]. As previously mentioned, the myocardium exhibits its greatest stiffness along the fiber direction $\mathbf{f}$, meaning we can model anisotropy under the assumption the material has a preferred direction in the reference configuration, from now on denoted by the unit vector $\mathbf{f}_0$. Therefore, two additional invariants can be defined as

$$I_4 = \mathbf{f}_0 \cdot (\mathbf{C}\mathbf{f}_0) \quad \text{and} \quad I_5 = \mathbf{f}_0 \cdot (\mathbf{C}^2 \mathbf{f}_0). \tag{2.14}$$

Similarly, if there are two preferred directions, the second denoted by $\mathbf{s}_0$, then this introduces the invariants

$$I_6 = \mathbf{s}_0 \cdot (\mathbf{C}\mathbf{s}_0) \quad \text{and} \quad I_7 = \mathbf{s}_0 \cdot (\mathbf{C}^2 \mathbf{s}_0). \tag{2.15}$$

Associated with it and, additionally, a coupling invariant, denoted by I_8, defined by

$$I_8 = \mathbf{f}_0 \cdot (\mathbf{C}\mathbf{s}_0) = \mathbf{s}_0 \cdot (\mathbf{C}\mathbf{f}_0). \tag{2.16}$$

Additionally, many models, including the one adopted in this work, consider splitting volumetric changes from distortional changes within the material. In this case, isochoric definitions of the deformation gradient are commonly used with corresponding changes to stretch tensors. In this case, we further decompose the deformation gradient $\mathbf{F}$ into volumetric ($\mathbf{F}_{\mathrm{vol}}$) and isochoric ($\bar{\mathbf{F}}$) parts, as $\mathbf{F} = \bar{\mathbf{F}}\mathbf{F}_{\mathrm{vol}}$ such that

$$\mathbf{F}_{\mathrm{vol}} = J^{\frac{1}{3}}\mathbf{I} \quad \text{and} \quad \bar{\mathbf{F}} = J^{-\frac{1}{3}}\mathbf{F}, \tag{2.17}$$

leading to the definiton of the modified right Cauchy-Green tensor

$$\bar{\mathbf{C}} = \bar{\mathbf{F}}^{\mathrm{T}}\bar{\mathbf{F}} = J^{-\frac{2}{3}}\mathbf{C}. \tag{2.18}$$

The reason for the decomposition of the deformation gradient $\mathbf{F}$ becomes clear once we introduce the constitutive law, particularly the strain energy function. Figure 2 provides a visual overview of the deformation mechanism of a solid body under the assumptions made throughout this Section.

---

[2]The trace operator on $\mathbf{A} \in \mathbb{R}^{d \times d}$ is defined as $\mathrm{trace}\,(\mathbf{A}) = \sum_i A_{ii}$
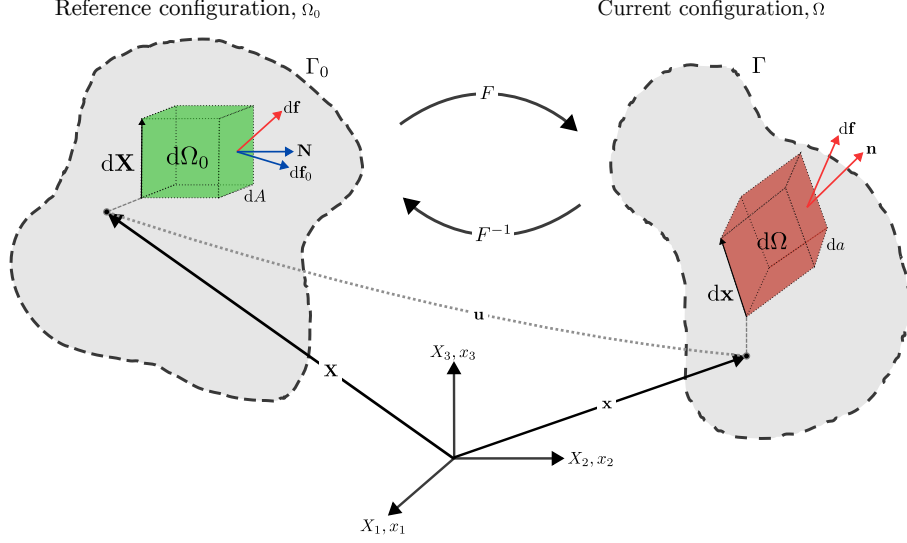
Figure 2: General motion of a deformable body. The figure shows the mapping from a reference configuration (Ω_0, Γ_0), with material coordinates $\mathbf{X}_i$, to a deformed configuration (Ω, Γ), with spatial coordinates $\mathbf{x}_i$. The deformation gradient tensor $\mathbf{F}$ maps differential vectors $d\mathbf{X}$ in the reference frame to $d\mathbf{x}$ in the deformed frame, characterizing local changes due to deformation. Illustrated in the domain is also a differential volume element, representing the mapping of forces (reference, $d\mathbf{f}_0$, and current, $d\mathbf{f}$) along with normals (reference, $\mathbf{N}$, and current, $\mathbf{n}$) and areas (reference, dA, and current, da).

2.1.2 Kinetics

Stress is a tensor variable that enables quantification of the internal tractions, meaning it describes the internal forces acting on a point in matter [11]. Cauchy postulated that a force on any surface that passes through a point depends only on its unit normal $\mathbf{n}$ [12]. To better understand the underlying mechanism of the Cauchy's stress theorem, let us consider a body $\mathscr{B}$ in the current configuration at a time t. In order to define the stress at some point P, let us further imagine a smooth surface Σ going through P and separating $\mathscr{B}$ into two parts (see Figure 3). Following the classical mechanics framework of Newton and Euler [13], external forces applied on the body are transmitted internally via contact forces and moments, generating internal stresses across Σ.

On an element of area ΔS containing P, with the outward unit normal vector $\mathbf{n}$, the internal action of one side of the body on the other is characterized by a force $\Delta \mathbf{F}$ and, in general, a moment $\Delta \mathbf{M}$. For classical continua, the moment $\Delta \mathbf{M}$ is assumed to vanish. As the area shrinks to a point, Cauchy's postulate assumes that the limit

$$\lim_{\Delta S \to 0} \frac{\Delta \mathbf{F}}{\Delta S} \tag{2.19}$$

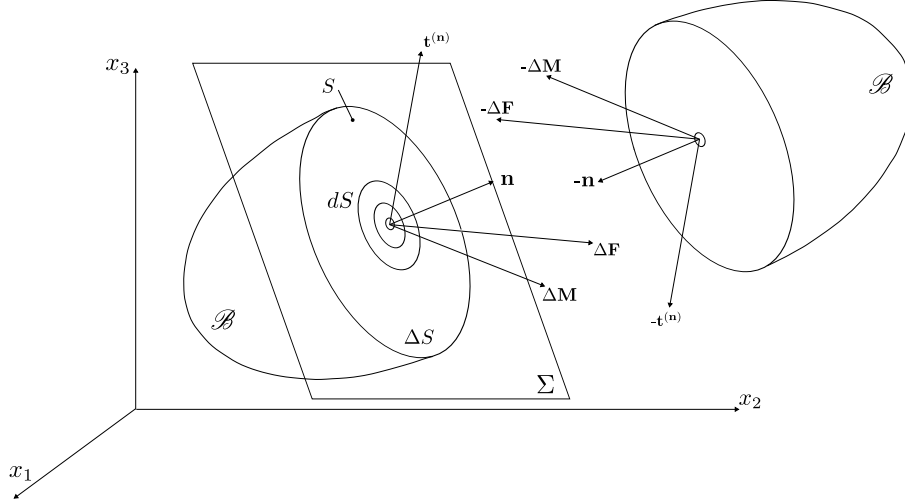exists and is finite, leading to the definition of the Cauchy traction vector $\mathbf{t}^{(\mathbf{n})}$.

Figure 3: Illustration of Cauchy's stress theorem. A smooth internal surface Σ is introduced through a point P of the body $\mathscr{B}$ in its current configuration. The surface divides the body into two parts, allowing the definition of internal forces $\Delta\mathbf{f}$ and moments $\Delta\mathbf{m}$ exerted across the interface. According to Cauchy's postulate, the traction vector $\mathbf{t}^{(\mathbf{n})}$ acting on the surface element ΔS depends purely on the orientation of its unit normal vector $\mathbf{n}$ at P. Vectors on opposing sides of the body are shown with opposite signs to represent the balance of internal forces and moments, consistent with Cauchy's stress theorem and Newton's third law.

This traction vector $\mathbf{t}^{(\mathbf{n})}$ depends on both the spatial position and the orientation of the surface. According to Cauchy's postulate, the traction vector is the same for all surfaces through P that share the same normal vector $\mathbf{n}$. Therefore, it can be written as a linear mapping from the space of normal vectors to force vectors.

Provided that $\mathbf{t}$ is a continuous function of position $\mathbf{x}$, the mapping $\mathbf{n} \mapsto \mathbf{t}$ must be linear, and so we define the Cauchy stress tensor $\boldsymbol{\sigma}$ such that:

$$\mathbf{t}^{(\mathbf{n})} = \boldsymbol{\sigma} \cdot \mathbf{n}, \qquad t_j^n = \sum_i \sigma_{ij} n_i. \tag{2.20}$$

This tensor $\boldsymbol{\sigma}$ characterizes the internal force distribution at a point in the current configuration of the body.

Depending on the orientation of the surface, the traction vector $\mathbf{t}^{(\mathbf{n})}$ may not be perpendicular to the plane on which it acts, as shown in Figure 4. Therefore, it can be decomposed into a normal component and a tangential component, defined respectively as

$$\sigma_n = \lim_{\Delta S \to 0} \frac{\Delta F_n}{\Delta S} = \frac{\mathrm{d}F_n}{\mathrm{d}S} \tag{2.21}$$

$$\tau_n = \lim_{\Delta S \to 0} \frac{\Delta F_s}{\Delta S} = \frac{\mathrm{d}F_s}{\mathrm{d}S}, \tag{2.22}$$

where $\mathrm{d}F_n$ is the component of force normal to the surface and $\mathrm{d}F_s$ is the component of force tangential to the surface.
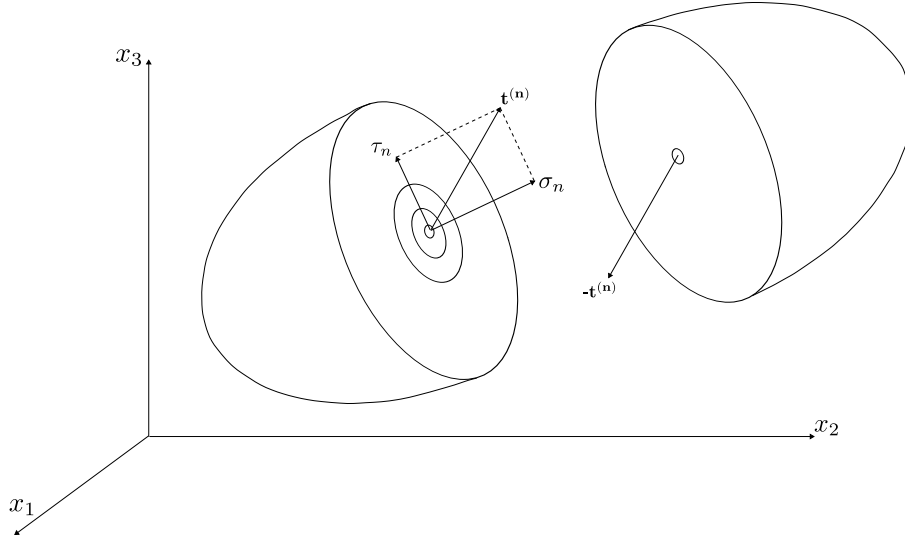
Figure 4: Decomposition of the traction vector $\mathbf{t^{(n)}}$ acting on an internal surface of orientation $\mathbf{n}$ into its normal and tangential components. The traction vector does not generally align with the normal vector and can be split into a normal stress σ_n, acting perpendicular to the surface, and a shear stress τ_n, acting tangentially.

By definition, the Cauchy stress is defined on the current configuration. However, the deformation gradient and strain tensors are described by relating the motion to the reference configuration. Thus, not all tensors describing the state of the material are in either the reference or current configuration [6]. Describing the stress, strain and deformation either in the reference or current configuration would make it easier to define constitutive models. To bypass this limitation, one can construct equivalent quantities to express the stress relative to the reference configuration. These are known as the first and second Piola–Kirchhoff stresses. The first Piola–Kirchhoff stress tensor, denoted by $\mathbf{P}$, satisfies $\frac{d\mathbf{f}}{dA} = \mathbf{PN}$ for all surfaces passing through the point on the reference configuration with normal $\mathbf{N}$ and surface area dA. Since $\mathbf{N}$ and dA are often more easily measured at the beginning of experiments, this form of stress can be more practical. $\mathbf{P}$ can be defined as

$$\mathbf{P} = J\boldsymbol{\sigma}\mathbf{F}^{-T}. \tag{2.23}$$

Because the first Piola–Kirchhoff $\mathbf{P}$ stress tensor relates forces in the current configuration with areas in the reference configuration, relating different coordinate systems, it is not symmetric. Alternatively, the second Piola–Kirchhoff stress tensor, $\mathbf{S}$, relates forces in the reference configuration to areas in the reference configuration. Therefore,

$$\mathbf{S} = J\mathbf{F}^{-1}\boldsymbol{\sigma}\mathbf{F}^{-T} \tag{2.24}$$

is a symmetric tensor. Since the relations are defined within the same configuration $(d\Omega_0)$, $\mathbf{S}$ is a convenient quantity for constitutive modelling.

2.1.3 Conservation Laws

To complete the mechanical description of deformable solids such as cardiac tissue, it is necessary to impose the physical conservation laws of mass and momentum [14, 11, 15]. The conservation of mass states that the mass of a body in a closed system can only be created or destroyed by a known source, which means we can assume that the material density is preserved as the myocardium deforms. It is written in the reference configuration as

$$\frac{D\rho J}{Dt} = \hat{\rho}J, \tag{2.25}$$

which states that the rate of change in mass, ρJ, is equal to the rate of mass being generated by a source $\hat{\rho}$. Here, $\frac{D}{Dt} = \frac{\partial}{\partial t} + \mathbf{v} \cdot \nabla$ defines the Lagrangian time derivative. For incompressible materials with constant density and no source of growth, the remaining mass balance equation is equivalent to $J - 1 = 0, \forall \mathbf{X} \in \Omega_0$.

Under the conditions of negligible acceleration and no body forces, the conservation of linear momentum simplifies to the null divergence of the first Piola–Kirchhoff stress tensor $\mathbf{P}$:

$$\mathrm{Div}\mathbf{P} = \mathbf{0}, \quad \forall \mathbf{X} \in \Omega_0. \tag{2.26}$$

This condition removes any dependency from the current configuration by forcing mechanical equilibrium in the reference configuration, and forms the foundation of the finite element formulation adopted in this work.

Finally, for completeness, the conservation of angular momentum states that the angular momentum of an isolated body remains constant in the absence of external forces. This translates to the requirement that the Cauchy stress tensor $\boldsymbol{\sigma}$ must remain symmetric under equilibrium conditions. In the current work, this is naturally satisfied through the use of the symmetric Cauchy stress tensor $\boldsymbol{\sigma}$.

3 Variational Formulation

3.1 Notation and assumptions

Let $\Omega \subset \mathbb{R}^d$ ($d = 2$ or 3) be a bounded Lipschitz domain with boundary decomposition $\partial\Omega = \Gamma^D \cup \Gamma^N$, where Γ^D has positive surface measure (otherwise the Dirichlet constraint is trivial). We denote by $\mathbf{u} : \Omega \to \mathbb{R}^d$ the displacement field, by $\mathbf{b} \in [L^2(\Omega)]^d$ the body force density, by $\mathbf{t} \in [L^2(\Gamma^N)]^d$ the prescribed traction, and by $\mathbf{u}_0$ the Dirichlet data on Γ^D.

Let us further consider a (linear) constitutive law of the form

$$\boldsymbol{\sigma}(\mathbf{u})(x) = \mathbb{C}(x) : \boldsymbol{\varepsilon}(\mathbf{u})(x), \tag{3.1}$$

where $\boldsymbol{\varepsilon}(\mathbf{u}) = \frac{1}{2}(\nabla\mathbf{u} + \nabla\mathbf{u}^T)$ is the (infinitesimal) strain tensor and $\mathbb{C}(x)$ is the fourth-order elasticity tensor. We assume $\mathbb{C}$ is measurable and satisfies the usual symmetry and ellipticity conditions: for a.e. $x \in \Omega$ and all symmetric matrices $\boldsymbol{E} \in \mathbb{R}^{d \times d}_{\mathrm{sym}}$,

$$\mathbb{C}_{ijkl}(x) = \mathbb{C}_{jikl}(x) = \mathbb{C}_{klij}(x) \quad \text{(symmetry)}, \tag{3.2}$$

$$\exists c_0 > 0 : \quad \mathbb{C}(x)\boldsymbol{E} : \boldsymbol{E} \geq c_0|\boldsymbol{E}|^2 \quad \text{(uniform positive definiteness)}, \tag{3.3}$$

and there exists $c_1 > 0$ such that

$$|\mathbb{C}(x)\boldsymbol{E} : \boldsymbol{F}| \leq c_1|\boldsymbol{E}|\,|\boldsymbol{F}| \quad \text{for all } \boldsymbol{E}, \boldsymbol{F}. \tag{3.4}$$

3.2 Weak form derivation

The equilibrium equations read

$$\begin{cases} \nabla \cdot \boldsymbol{\sigma}(\mathbf{u}) + \mathbf{b} = \mathbf{0} & \text{in } \Omega, \\ \boldsymbol{\sigma}(\mathbf{u}) \cdot \mathbf{n} = \mathbf{t} & \text{on } \Gamma^N, \\ \mathbf{u} = \mathbf{u}_0 & \text{on } \Gamma^D. \end{cases} \tag{3.5}$$

We now derive the variational formulation by multiplying the PDE by a test function and integrating over the domain, Ω.

Let $\mathbf{v} \in [C_c^\infty(\overline{\Omega} \setminus \Gamma^D)]^d$ be a smooth test function vanishing on Γ^D. Multiplying (3.5) by $\mathbf{v}$ and integrating over Ω:

$$\int_\Omega (\nabla \cdot \boldsymbol{\sigma}(\mathbf{u})) \cdot \mathbf{v} \, dx + \int_\Omega \mathbf{b} \cdot \mathbf{v} \, dx = 0.$$

For a tensor field $\boldsymbol{\sigma}$ and vector $\mathbf{v}$,

$$(\nabla \cdot \boldsymbol{\sigma}) \cdot \mathbf{v} = \nabla \cdot (\boldsymbol{\sigma}\mathbf{v}) - \boldsymbol{\sigma} : \nabla \mathbf{v},$$

where $\boldsymbol{\sigma} : \nabla \mathbf{v} = \sum_{i,j} \sigma_{ij} \partial_j v_i$. Integrating and applying the divergence theorem:

$$\begin{aligned}
\int_\Omega (\nabla \cdot \boldsymbol{\sigma}) \cdot \mathbf{v} \, dx &= \int_{\partial\Omega} (\boldsymbol{\sigma}\mathbf{v}) \cdot \mathbf{n} \, ds - \int_\Omega \boldsymbol{\sigma} : \nabla \mathbf{v} \, dx \\
&= \int_{\partial\Omega} (\boldsymbol{\sigma} \cdot \mathbf{n}) \cdot \mathbf{v} \, ds - \int_\Omega \boldsymbol{\sigma} : \nabla \mathbf{v} \, dx.
\end{aligned}$$

Using the boundary conditions and the fact that $\mathbf{v} = \mathbf{0}$ on Γ^D,

$$\int_\Omega (\nabla \cdot \boldsymbol{\sigma}) \cdot \mathbf{v} \, dx = \int_{\Gamma^N} \mathbf{t} \cdot \mathbf{v} \, ds - \int_\Omega \boldsymbol{\sigma} : \nabla \mathbf{v} \, dx.$$

Thus the weak form reads

$$-\int_\Omega \boldsymbol{\sigma}(\mathbf{u}) : \nabla \mathbf{v} \, dx + \int_{\Gamma^N} \mathbf{t} \cdot \mathbf{v} \, ds + \int_\Omega \mathbf{b} \cdot \mathbf{v} \, dx = 0. \tag{3.6}$$

Because $\boldsymbol{\sigma}$ is symmetric and $\boldsymbol{\varepsilon}(\mathbf{v}) = \frac{1}{2}(\nabla \mathbf{v} + \nabla \mathbf{v}^T)$, one can symmetrize:

$$\boldsymbol{\sigma} : \nabla \mathbf{v} = \boldsymbol{\sigma} : \boldsymbol{\varepsilon}(\mathbf{v}) \quad \text{whenever } \boldsymbol{\sigma} \text{ is symmetric,}$$

so (3.6) becomes

$$\int_\Omega \mathbb{C}\boldsymbol{\varepsilon}(\mathbf{u}) : \boldsymbol{\varepsilon}(\mathbf{v}) \, dx = \int_\Omega \mathbf{b} \cdot \mathbf{v} \, dx + \int_{\Gamma^N} \mathbf{t} \cdot \mathbf{v} \, ds. \tag{3.7}$$

3.3 Functional spaces

Define

$$H^1(\Omega; \mathbb{R}^d) = \{\mathbf{v} : \Omega \to \mathbb{R}^d \mid v_i \in H^1(\Omega) \; \forall i\},$$

and the subspace

$$V := \{\mathbf{v} \in H^1(\Omega; \mathbb{R}^d) : \mathbf{v} = \mathbf{0} \text{ on } \Gamma^D\}.$$

Given nonhomogeneous Dirichlet data $\mathbf{u}_0$ with a lifting $\mathbf{u}_D \in H^1(\Omega; \mathbb{R}^d)$ such that $\mathbf{u}_D|_{\Gamma^D} = \mathbf{u}_0$, the solution is sought as $\mathbf{u} = \mathbf{u}_D + \mathbf{w}$ with $\mathbf{w} \in V$ satisfying

$$\boxed{a(\mathbf{w}, \mathbf{v}) = F(\mathbf{v}) \quad \forall \mathbf{v} \in V,} \tag{3.8}$$

where

$$a(\mathbf{u}, \mathbf{v}) := \int_\Omega \mathbb{C}\boldsymbol{\varepsilon}(\mathbf{u}) : \boldsymbol{\varepsilon}(\mathbf{v}) \, dx, \tag{3.9}$$

$$F(\mathbf{v}) := \int_\Omega \mathbf{b} \cdot \mathbf{v} \, dx + \int_{\Gamma^N} \mathbf{t} \cdot \mathbf{v} \, ds - a(\mathbf{u}_D, \mathbf{v}). \tag{3.10}$$

Remark 3.1. *The use of $\boldsymbol{\varepsilon}(\mathbf{v})$ is essential both physically (since stress is symmetric) and analytically (since Korn's inequality controls the H^1-norm by $\|\boldsymbol{\varepsilon}(\cdot)\|_{L^2}$).*

3.4 Boundedness and coercivity of the bilinear form

3.4.1 Continuity

From (3.4) and Cauchy–Schwarz:

$$\begin{aligned}
|a(\mathbf{u},\mathbf{v})| = \left| \int_\Omega \mathbb{C}\varepsilon(\mathbf{u}) : \varepsilon(\mathbf{v})\,dx \right| \\
\leq c_1 \int_\Omega |\varepsilon(\mathbf{u})|\,|\varepsilon(\mathbf{v})|\,dx \\
\leq c_1 \|\varepsilon(\mathbf{u})\|_{L^2(\Omega)}\|\varepsilon(\mathbf{v})\|_{L^2(\Omega)} \\
\leq C_{\text{cont}} \|\mathbf{u}\|_{H^1(\Omega)}\|\mathbf{v}\|_{H^1(\Omega)}.
\end{aligned}$$

Thus $a(\cdot,\cdot)$ is continuous on $V \times V$. Here, we implicity used the norm equivalence defined as

$$\|\varepsilon(\mathbf{u})\|_{L^2(\Omega)} \leq \|\nabla\mathbf{u}\|_{L^2(\Omega)} \leq \|\mathbf{u}\|_{H^1(\Omega)}$$

.

3.4.2 Coercivity

From (3.3) and Korn's inequality:

$$a(\mathbf{v},\mathbf{v}) = \int_\Omega \mathbb{C}\varepsilon(\mathbf{v}) : \varepsilon(\mathbf{v})\,dx \geq c_0 \|\varepsilon(\mathbf{v})\|^2_{L^2(\Omega)},$$
$$\|\mathbf{v}\|_{H^1(\Omega)} \leq C_K \|\varepsilon(\mathbf{v})\|_{L^2(\Omega)}.$$

Hence

$$a(\mathbf{v},\mathbf{v}) \geq \frac{c_0}{C_K^2} \|\mathbf{v}\|^2_{H^1(\Omega)},$$

so $a(\cdot,\cdot)$ is coercive on V, with c_0 and C_K depending only on Ω.

3.5 Boundedness of the linear functional

For $\mathbf{b} \in [L^2(\Omega)]^d$, $\mathbf{t} \in [L^2(\Gamma^N)]^d$, and $\mathbf{u}_D \in H^1(\Omega)$,

$$\begin{aligned}
|F(\mathbf{v})| \leq \|\mathbf{b}\|_{L^2(\Omega)}\|\mathbf{v}\|_{L^2(\Omega)} + \|\mathbf{t}\|_{L^2(\Gamma^N)}\|\mathbf{v}\|_{L^2(\Gamma^N)} + |a(\mathbf{u}_D,\mathbf{v})| \\
\leq C_1 \|\mathbf{v}\|_{H^1(\Omega)}.
\end{aligned}$$

Thus $F \in V'$.

3.6 Existence and uniqueness

Theorem 3.2 (Existence and uniqueness). *Under assumptions* (3.3)–(3.4) *with* Γ^D *of positive measure, there exists a unique* $\mathbf{w} \in V$ *such that*

$$a(\mathbf{w},\mathbf{v}) = F(\mathbf{v}) \quad \forall \mathbf{v} \in V.$$

Consequently $\mathbf{u} = \mathbf{u}_D + \mathbf{w}$ *is the unique weak solution in* $\mathbf{u}_D + V \subset H^1(\Omega;\mathbb{R}^d)$ *of* (3.5).

Proof. By continuity and coercivity of $a(\cdot,\cdot)$ and continuity of F, the Lax–Milgram theorem applies directly. $\square$

4 Finite Element Discretization

The weak form of the equilibrium equation can be stated as: find the displacement field $\mathbf{u} \in \mathcal{V}$ such that

$$a(\mathbf{u}, \mathbf{v}) = L(\mathbf{v}) \quad \forall \mathbf{v} \in \mathcal{V}_0, \tag{4.1}$$

where the bilinear and linear forms are defined by

$$a(\mathbf{u}, \mathbf{v}) = \int_{\Omega_0} \boldsymbol{\sigma}(\mathbf{u}) : \nabla \mathbf{v} \, \mathrm{d}V, \tag{4.2}$$

$$L(\mathbf{v}) = \int_{\Omega_0} \mathbf{b}_0 \cdot \mathbf{v} \, \mathrm{d}V + \int_{\Gamma_t} \mathbf{t}_0 \cdot \mathbf{v} \, \mathrm{d}A. \tag{4.3}$$

Here, Ω_0 denotes the reference configuration, Γ_t the Neumann boundary, and $\mathcal{V}, \mathcal{V}_0$ are appropriate Sobolev spaces for admissible and test displacements, respectively.

4.1 Domain Discretization

The reference domain Ω_0 is partitioned into N_e non-overlapping finite elements Ω_e:

$$\overline{\Omega}_0 = \bigcup_{e=1}^{N_e} \overline{\Omega}_e.$$

Within each element, the displacement field is approximated by a finite-dimensional expansion:

$$\mathbf{u}_h(\mathbf{X}) = \sum_{i=1}^{N_n} \mathbf{N}_i(\mathbf{X}) \, \mathbf{d}_i, \tag{4.4}$$

where $\mathbf{N}_i$ are the vector-valued shape functions associated with node i, $\mathbf{d}_i$ are the nodal displacement vectors, and N_n is the total number of nodes.

The test function $\mathbf{v}$ is approximated analogously as

$$\mathbf{v}_h(\mathbf{X}) = \sum_{i=1}^{N_n} \mathbf{N}_i(\mathbf{X}) \, \boldsymbol{\eta}_i, \tag{4.5}$$

where $\boldsymbol{\eta}_i$ represent arbitrary virtual nodal displacements. The shape functions satisfy the standard Kronecker delta property:

$$\mathbf{N}_i(\mathbf{X}_j) = \delta_{ij}.$$

4.2 Discretized Weak Form

Substituting (4.4)–(4.5) into the weak form (4.1) yields the discrete problem: find $\mathbf{u}_h \in \mathcal{V}_h$ such that

$$a(\mathbf{u}_h, \mathbf{v}_h) = L(\mathbf{v}_h) \quad \forall \mathbf{v}_h \in \mathcal{V}_h, \tag{4.6}$$

where $\mathcal{V}_h \subset \mathcal{V}$ is the finite-dimensional subspace spanned by the chosen shape functions.

Expanding in nodal form:

$$\sum_{i=1}^{N_n} \sum_{j=1}^{N_n} \boldsymbol{\eta}_i \cdot \left[\int_{\Omega_0} (\nabla \mathbf{N}_i)^{\mathsf{T}} \mathbf{C}(\mathbf{u}_h) \, \nabla \mathbf{N}_j \, \mathrm{d}V \right] \mathbf{d}_j = \sum_{i=1}^{N_n} \boldsymbol{\eta}_i \cdot \left[\int_{\Omega_0} \mathbf{N}_i^{\mathsf{T}} \mathbf{b}_0 \, \mathrm{d}V + \int_{\Gamma_t} \mathbf{N}_i^{\mathsf{T}} \mathbf{t}_0 \, \mathrm{d}A \right], \quad \tag{4.7}$$

where $\mathbf{C}(\mathbf{u}_h)$ is the material tangent operator obtained from the constitutive law $\boldsymbol{\sigma}(\mathbf{u}_h)$.

4.3 Matrix Formulation

Because the coefficients $\boldsymbol{\eta}_i$ are arbitrary, we obtain the discrete algebraic system:

$$\mathbf{K}(\mathbf{u}_h)\,\mathbf{d} = \mathbf{f}, \tag{4.8}$$

with

$$\mathbf{K}(\mathbf{u}_h) = \int_{\Omega_0} \mathbf{B}^\mathsf{T}\,\mathbf{C}(\mathbf{u}_h)\,\mathbf{B}\,\mathrm{d}V, \tag{4.9}$$

$$\mathbf{f} = \int_{\Omega_0} \mathbf{N}^\mathsf{T}\,\mathbf{b}_0\,\mathrm{d}V + \int_{\Gamma_t} \mathbf{N}^\mathsf{T}\,\mathbf{t}_0\,\mathrm{d}A, \tag{4.10}$$

where $\mathbf{B}$ is the strain–displacement matrix.

Equation (4.8) represents a nonlinear algebraic system in the unknown nodal displacements $\mathbf{d}$ due to the dependence of $\mathbf{K}$ on $\mathbf{u}_h$.

4.4 Nonlinear Solution Procedure

In nonlinear elasticity, the internal force vector depends on the current configuration. The equilibrium condition can be expressed as

$$\mathbf{r}(\mathbf{d}) = \mathbf{f}_{\text{ext}} - \mathbf{f}_{\text{int}}(\mathbf{d}) = \mathbf{0}.$$

Using the Newton–Raphson method, the linearized form at iteration k is

$$\mathbf{K}_{\text{T}}^{(k)}\,\Delta\mathbf{d}^{(k)} = \mathbf{r}^{(k)}, \tag{4.11}$$

where $\mathbf{K}_{\text{T}}^{(k)}$ is the tangent stiffness matrix and $\mathbf{r}^{(k)}$ is the residual vector. The displacement field is then updated as

$$\mathbf{d}^{(k+1)} = \mathbf{d}^{(k)} + \Delta\mathbf{d}^{(k)},$$

until convergence criteria are met. For more details on the implementation of the Newton–Raphson method in nonlinear finite element analysis, refer to [16, 6].

4.5 Summary
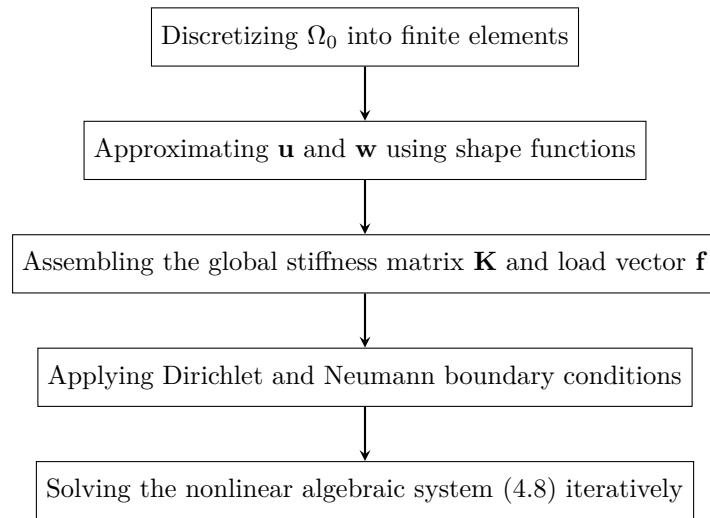
Figure 5: Steps involved in the numerical process.

In the next section we show the `FEniCS` implementation of the above theory for the problem at hand.

5   Implementation in `FEniCS`

The finite element solution of the equilibrium equations (3.5) was implemented in `FEniCS`[3] following the variational formulation (3.8). At each loading step, the displacement field $\mathbf{u}_h \in V_h \subset V$ was obtained as the solution of the discrete weak problem

$$a(\mathbf{u}_h, \mathbf{v}_h) = F(\mathbf{v}_h) \quad \forall \, \mathbf{v}_h \in V_h,$$

where $a(\cdot, \cdot)$ and $F(\cdot)$ are the bilinear and linear forms defined in (3.9)–(3.10). This discrete system corresponds to a nonlinear algebraic problem of the form

$$\mathbf{R}(\mathbf{u}_h) = \mathbf{0},$$

which was solved iteratively using a Newton–Raphson scheme until convergence of the residual norm, whose underlying mechanism is briefly described in Section 4.4. The complete `FEniCS` implementation is available in **GitHub**[4], while only the key steps are shown here for clarity.

Initially, a continuous, piecewise-linear vector space V_h was defined as

```
# Function space for displacement (vector field)
V = VectorFunctionSpace(mesh, 'P', 1)
```

to approximate the displacement field $\mathbf{u}_h \in V_h \subset [H^1(\Omega)]^3$. The Dirichlet condition $\mathbf{u} = \mathbf{0}$ on Γ^D was imposed as

```
# Initial conditions and boundary conditions
boundaries = boundary_markers
zero_displacement = Constant(("0.0", "0.0", "0.0"))

# Homogeneous Dirichlet BC on the base
bcr = DirichletBC(W.sub(0),
                  zero_displacement,
                  boundaries,
                  numbering['BASE']
                  )
bcs = [bcr]
```

The discrete weak form corresponding to Eq. (3.7) was defined as

```
# Define functions (trial function w)
w = Function(W)
(u, p) = split(w)
(v, q) = TestFunctions(W)

eq = inner(P,grad(v))*dx + inner(J-1,q)*dx + dot(J*inv(F).T*n_mesh*p0, v)*
ds(numbering['ENDO'])
Jac = derivative(eq, w)
```

The nonlinear equilibrium problem $F(\mathbf{u}_h) = 0$ was solved using Newton's method, whose underlying mechanism is briefly described in Section 4.4, by defining the problem and solver as:

```
problem = NonlinearVariationalProblem(F, u, bcs, J=Jac)
solver = NonlinearVariationalSolver(problem)
solver.parameters['newton_solver']['relative_tolerance'] = 1e-6
solver.parameters['newton_solver']['maximum_iterations'] = 50

solver.solve()
```

The Green–Lagrange strain $\mathbf{E}$ and the 2nd Piola–Kirchhoff stress $\mathbf{S}$ are computed post-solution to verify the internal response of the material

---

[3]For more details on this software, the reader is referred to [17, 18].

[4]`https://github.com/DiogoAmaro13/FEM-Implementation-for-Passive-Diastolic-Filling.git`

```
1    F = Identity(3) + grad(u)
2    E = 0.5 * (F.T*F - Identity(3))
3    S = lmbda*tr(E)*Identity(3) + 2*mu*E
4
5    eps = project(E, TensorFunctionSpace(mesh, 'P', 1))
6    PK2 = project(S, TensorFunctionSpace(mesh, 'P', 1))
```

and exported for appropriate visualization.

6 Results

labelresults The finite element implementation described in Section 5 was executed on the LV geometry, discretized with a tetrahedral mesh. The model was subjected to an increasing endo-cardial pressure load, applied over 20 incremental steps, representing a gradual filling process. At each iteration step, the nonlinear equilibrium problem

$$\mathbf{R}(\mathbf{u}_h) = \mathbf{0},$$

was solved using a Newton–Raphson procedure, and the resulting fields were post-processed and exported for visualization.

The implementation produces three primary output fields at each iteration step:

a) The displacement field $\mathbf{u}_h$, representing the nodal deformation of the LV mesh under internal pressure, i.e., the total deformation of the reference configuration Ω_0;

b) The Green–Lagrange strain tensor $\mathbf{E}_h = \frac{1}{2}(\mathbf{F}^\mathsf{T}\mathbf{F} - \mathbf{I})$, which quantifies the local finite deformation in the material configuration;

c) The Second Piola–Kirchhoff stress tensor $\mathbf{S}_h$ obtained from the constitutive relation $\mathbf{S}_h = \mathbb{C} : \mathbf{E}_h$, representing the internal stress response.

Each field was saved in `.pvd` format and visualized using `ParaView`. Figures 6–8 display the evolution of the displacement, strain, and stress distributions across the cardiac wall over four equidistant loading steps. The displacement field exhibited a progressive increase in magnitude from the base (Dirichlet boundary Γ^D) to the apex under the prescribed pressure on Γ^N, as expected from the applied loading. The stress distribution showed higher values near the endocardial surface, consistent with the mechanical response of the LV wall under internal pressure.
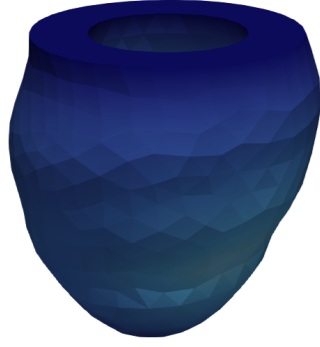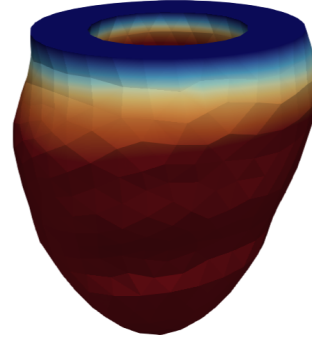
(a) Initial state: $p = 0$ mmHg
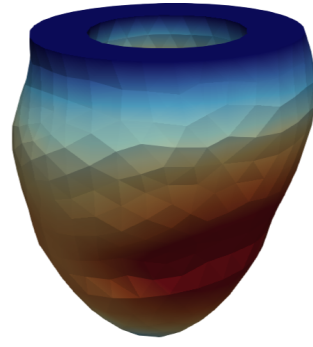
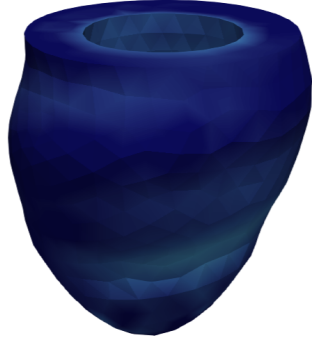(b) 7th iteration: $p = 0.467$ mmHg
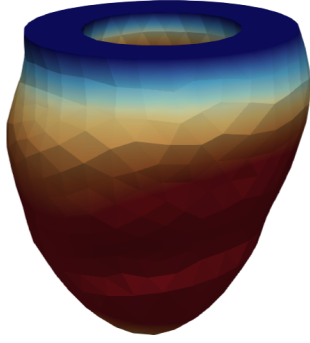
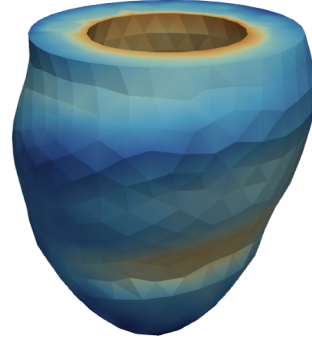(c) 14th iteration: $p = 0.933$ mmHg
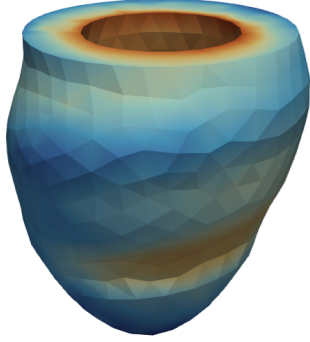
(d) Final state: $p = 1.330$ mmHg

Figure 6: Displacement field $\mathbf{u}_h$ at selected loading steps. The largest displacements are observed near the apex (represented by warmer colors), while the base remains fixed due to Dirichlet boundary conditions (colder colors). The color scale is kept constant across panels to enable direct comparison of deformation amplitude with increasing internal pressure.

(a) Initial state: $p = 0$ mmHg

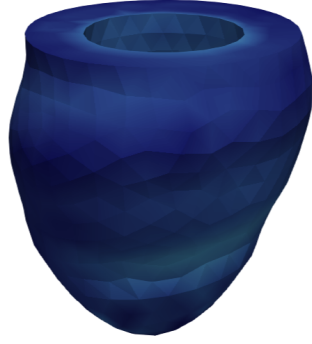(b) 7th iteration: $p = 0.467$ mmHg
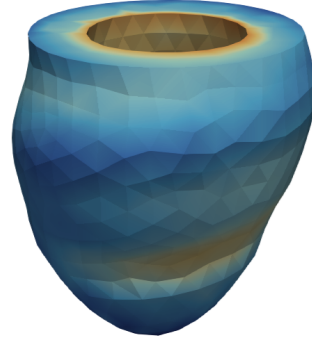
(c) 14th iteration: $p = 0.933$ mmHg
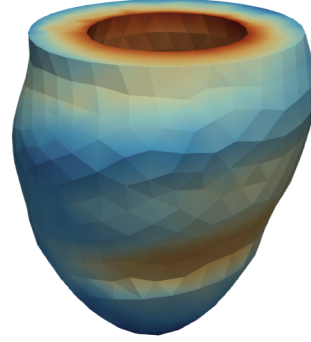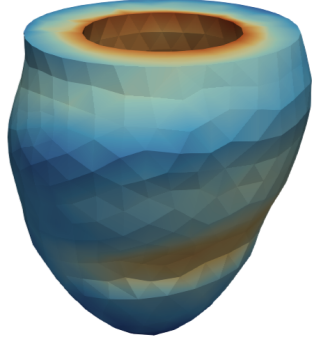
(d) Final state: $p = 1.330$ mmHg

Figure 7: Strain magnitude at selected loading steps. The strain field is typically higher at the endocardial surface and decreases toward the epicardium, consistent with the pressure-driven wall deformation. The color map is preserved across panels for visual consistency.
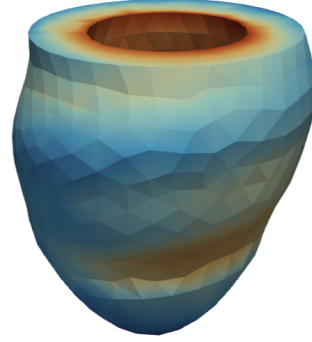
(a) Initial state: $p = 0$ mmHg

(b) 7th iteration: $p = 0.467$ mmHg

(c) 14th iteration: $p = 0.933$ mmHg

(d) Final state: $p = 1.330$ mmHg

Figure 8: Stress distribution in the ventricular wall at selected loading steps. Stress concentrates near the endocardial surface where the internal pressure is applied. As the pressure increases, the magnitude of stress rises and the high-stress region near the endocardium becomes more pronounced. The color scale is kept fixed across panels for quantitative comparison.

Additionally, the computed cavity volume at each iteration step allows the construction of the pressure–volume (PV) curve shown in Figure 9. This curve provides a global measure of the model's mechanical response to progressive pressure loading.
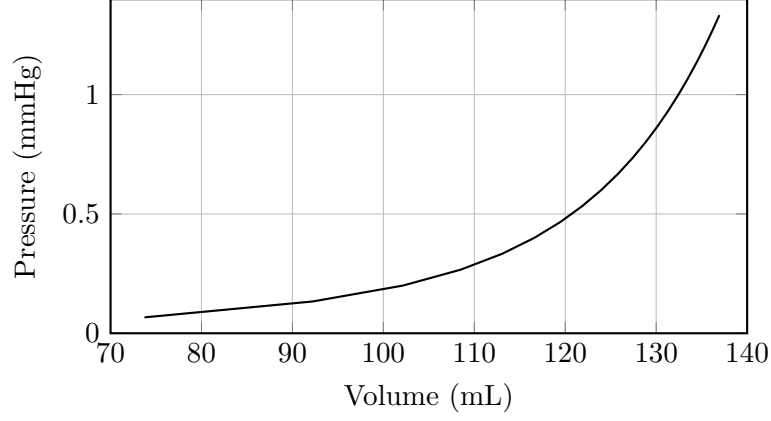
Figure 9: Pressure as a funtion of volume during the passive filling of the LV.

This curve further validates the numerical implementation by demonstrating an exponential relation between pressure and volume, characteristic of passive ventricular filling mechanics [19].

Additionally, during the cardiac cycle, the apex and base of the heart rotate in opposite directions. This behavior is caused by the specific layering of fibers. In the LV, fibers in the epicardium run in a left-handed direction, fibers in the mid layer run circumferentially, and fibers in the endocardium run in a right-handed direction [20]. Because these fiber groups are actively connected and activated together, their contraction leads not only to radial and longitudinal deformation, but also to a net rotational effect [21]. The specific myofibre orientation associated with the epicardium will cause the base to rotate in a clockwise direction and the apex to rotate in a counterclockwise direction, while the contraction of myocardial fibers on the endocardial side will cause the base to rotate in a counterclockwise direction and the apex to rotate in a clockwise direction. This means that rotations caused by the epicardium and endocardium are always in opposite directions.
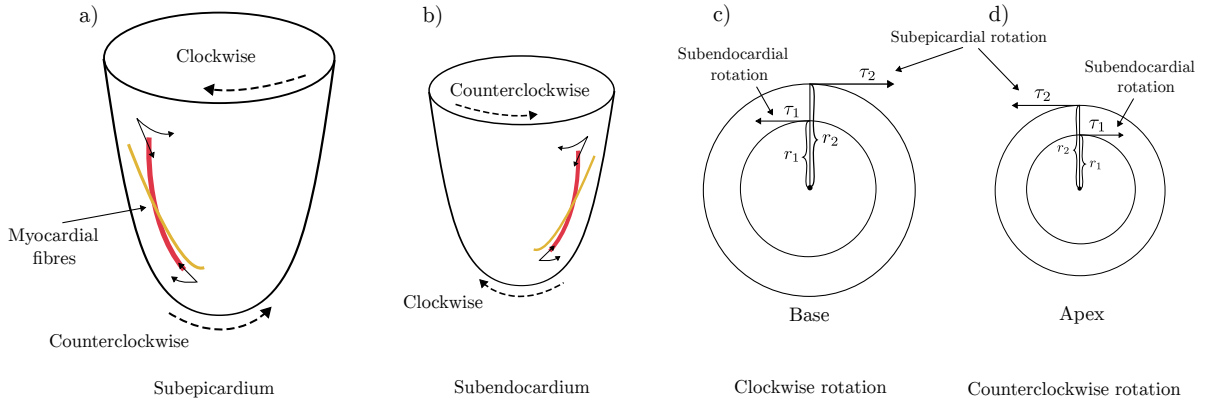

Figure 10: Myocardial contraction and opposite rotation at the base and apex. (a) When myocardial fibers on the subepicardial side contract, clockwise rotational torque is produced at the base and counterclockwise rotational torque at the apex. (b) When myocardial fibers on the subendocardial side contract, counterclockwise rotational torque is produced at the base and clockwise rotational torque at the apex. (c) Subepicardial radius is larger than subendocardial radius ($r_2 > r_1$). (d) Therefore, subepicardial rotational torque is larger than subendocardial rotational torque ($\tau_2 > \tau_1$). Adapted from [21].

While the present work focuses on modelling the passive filling phase, and does not explic-

itly simulates the torsion mechanism of the LV, it is still important to have a context of this mechanism, mainly because of two reasons. Firstly, and from a physiological standpoint, it is well defined that the degree of shortening of myocardial fibers is of the order of 15-20%, at most [22]. If ejection was simply the result of contraction of myocardial fibers, the ejection fraction would be 15-20%, whereas the actual ejection fraction of the human heart is 60-70% [23]. This is due to the involvement of twisting. Myocardial fibers are oriented in a spherical way, so that when they contract they cause a simultaneous wringing action, resulting in an ejection fraction of 60-70%. In addition, after twisting has occurred during systole, untwisting occurs during diastole. Untwisting is known to occur mostly during the relaxation phase, suggesting that this motion assists LV relaxation, which directly influences the mechanism being studied in this work. Therefore, we can further validate our implementation by observing the direction and general orientation of the displacement field during the passive filling phase. Figure 11 shows the displacement field with arrows indicating the direction of displacement at various points in the LV wall.
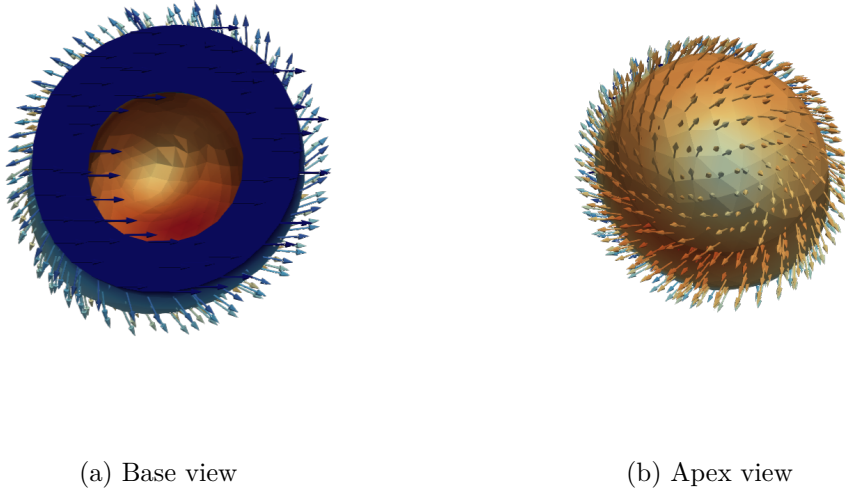

(a) Base view (b) Apex view

Figure 11: Displacement field $\mathbf{u}_h$ at final loading step with arrows indicating the direction of displacement. This representation was obtained using ParaView's `Glyph` filter to visualize the orientation of the displacement vectors. The arrows near the apex indicate a counterclockwise rotation, while those near the base indicate a clockwise rotation, consistent with the physiological torsion mechanism explained above.

7 Discussion

The numerical results presented in Section **??** demonstrate that the discrete displacement field $\mathbf{u}_h$ satisfies the weak equilibrium equation (3.7) within numerical tolerance. In particular, the balance of internal and external virtual work,

$$a(\mathbf{u}_h, \mathbf{v}_h) = F(\mathbf{v}_h) \quad \forall \, \mathbf{v}_h \in V_h,$$

is enforced at every loading step, confirming that the computed $\mathbf{u}_h$ is, in fact, an admissible weak solution to the governing PDEs. To further verify this equilibrium, we evaluated the residual of the weak form

$$\int_\Omega \mathbf{P} : \nabla \mathbf{v} \, d\Omega + \int_\Omega (J - 1) \, q \, d\Omega - \int_{\Gamma_{\text{endo}}} p_0 (\mathbf{J} \mathbf{F}^{-T} \mathbf{n}) \cdot \mathbf{v} \, d\Gamma = 0$$

20

for a random set of admissible test functions $\mathbf{v}$. The resulting residual value was on the order of 10^{-10}, further validating our numerical solution.

Moreover, and although achieving full physiological accuracy was not the main goal of this work, the results show strong biomechanical plausibility. The PV relationship in Figure 9 exhibits the characteristic nonlinear stiffening behavior of passive myocardium, where pressure and volume exhibit a clear exponential relationship [24, 25].

The deformation and stress patterns in Figures 6–8 show that the left ventricle expands primarily in the radial direction under internal pressure, with negligible displacement at the basal region due to Dirichlet boundary constraints. Stress concentrations are observed near the endocardial surface, where the applied pressure acts, while the epicardial layers experience lower stress magnitudes. Similarly, the strain field exhibits higher values in those same endocardial regions, confirming mechanical coherence between stress and strain responses.[5]

Finally, the consistency between the weak-form residual, the smooth stress–strain fields, and the reasonable PV response indicates that the finite element formulation, implementation, and boundary conditions together converge in a valid and numerical approximation of the deformation problem studied in this work.

Future developments may include coupling the current passive model with an active tension formulation to simulate the full cardiac cycle, as well as incorporating subject-specific geometries and fiber architectures derived from medical imaging, which would provide a more accurate representation of left ventricular mechanics, particularly if the goal is patient-specific simulations.

---

[5]Stress quantifies the internal resistance to deformation (force per area), while strain measures the geometric deformation (stretch, shear, contraction) itself.

References

[1] G. A. Holzapfel and R. W. Ogden, "Constitutive modelling of passive myocardium: a structurally based framework for material characterization," *Philosophical Transactions of the Royal Society A: Mathematical, Physical and Engineering Sciences*, vol. 367, no. 1902, pp. 3445–3475, 2009.

[2] U. Noè, A. Lazarus, H. Gao, V. Davies, B. Macdonald, K. Mangion, C. Berry, X. Luo, and D. Husmeier, "Gaussian process emulation to accelerate parameter estimation in a mechanical model of the left ventricle: a critical step towards clinical end-user relevance," *Journal of the Royal Society Interface*, vol. 16, no. 156, p. 20190114, 2019.

[3] Y.-c. Fung, "A first course in continuum mechanics," *Englewood Cliffs*, 1977.

[4] M. E. Gurtin, *An introduction to continuum mechanics*, vol. 158. Academic press, 1982.

[5] L. E. Malvern, *Introduction to the Mechanics of a Continuous Medium.* No. Monograph, 1969.

[6] J. Bonet and R. D. Wood, *Nonlinear continuum mechanics for finite element analysis.* Cambridge university press, 1997.

[7] M. Zeidi and C. I. Kim, "Mechanics of an elastic solid reinforced with bidirectional fiber in finite plane elastostatics: complete analysis," *Continuum Mechanics and Thermodynamics*, vol. 30, no. 3, pp. 573–592, 2018.

[8] R. W. Ogden, *Non-linear elastic deformations.* Courier Corporation, 1997.

[9] A. Spencer, "Continuum mechanics (dover books on physics)," 2004.

[10] G. A. Holzapfel and N.-l. S. Mechanics, "A continuum approach for engineering," 2000.

[11] G. A. Holzapfel, "Nonlinear solid mechanics: a continuum approach for engineering science," 2002.

[12] W. Noll, "Lectures on the foundations of continuum mechanics and thermodynamics," *Archive for Rational Mechanics and Analysis*, vol. 52, pp. 62–92, 1973.

[13] C. Truesdell, W. Noll, C. Truesdell, and W. Noll, *The non-linear field theories of mechanics.* Springer, 2004.

[14] A. Quarteroni, A. Manzoni, C. Vergara, *et al.*, *Mathematical modelling of the human cardiovascular system: data, numerical approximation, clinical applications*, vol. 33. Cambridge University Press, 2019.

[15] D. Chapelle, J.-F. Gerbeau, J. Sainte-Marie, and I. Vignon-Clementel, "A poroelastic model valid in large strains with applications to perfusion in cardiac modeling," *Computational Mechanics*, vol. 46, pp. 91–101, 2010.

[16] O. C. Zienkiewicz and R. L. Taylor, *The finite element method for solid and structural mechanics.* Elsevier, 2005.

[17] A. Logg, K.-A. Mardal, and G. Wells, *Automated solution of differential equations by the finite element method: The FEniCS book*, vol. 84. Springer Science & Business Media, 2012.

[18] M. Alnæs, J. Blechta, J. Hake, A. Johansson, B. Kehlet, A. Logg, C. Richardson, J. Ring, M. E. Rognes, and G. N. Wells, "The fenics project version 1.5," *Archive of numerical software*, vol. 3, no. 100, 2015.

[19] J. Humphrey and F. Yin, "On constitutive relations and finite deformations of passive cardiac tissue: I. a pseudostrain-energy function," 1987.

[20] G. Buckberg, A. Mahajan, S. Saleh, J. I. Hoffman, and C. Coghlan, "Structure and function relationships of the helical ventricular myocardial band," *The Journal of thoracic and cardiovascular surgery*, vol. 136, no. 3, pp. 578–589, 2008.

[21] S. Nakatani, "Left ventricular rotation and twist: why should we learn?," *Journal of cardiovascular ultrasound*, vol. 19, no. 1, p. 1, 2011.

[22] S.-J. Dong, P. S. Hees, C. O. Siu, J. L. Weiss, and E. P. Shapiro, "Mri assessment of lv relaxation by untwisting rate: a new isovolumic phase measure of τ," *American Journal of Physiology-Heart and Circulatory Physiology*, vol. 281, no. 5, pp. H2002–H2009, 2001.

[23] M. T. Maeder and D. M. Kaye, "Heart failure with normal left ventricular ejection fraction," *Journal of the American College of Cardiology*, vol. 53, no. 11, pp. 905–918, 2009.

[24] S. Klotz, I. Hay, M. L. Dickstein, G.-H. Yi, J. Wang, M. S. Maurer, D. A. Kass, and D. Burkhoff, "Single-beat estimation of end-diastolic pressure-volume relationship: a novel method with potential for noninvasive application," *American Journal of Physiology-Heart and Circulatory Physiology*, vol. 291, no. 1, pp. H403–H412, 2006.

[25] D. Burkhoff, I. Mirsky, and H. Suga, "Assessment of systolic and diastolic ventricular properties via pressure-volume analysis: a guide for clinical, translational, and basic researchers," *American Journal of Physiology-Heart and Circulatory Physiology*, 2005.